100-period InGaAsP/InGaP Superlattice Solar Cell with Sub-bandgap Quantum Efficiency Approaching 80%

Islam E. H. Sayed[1,2], Nikhil Jain[2], Myles A. Steiner[2], John F. Geisz[2], S. M. Bedair[1]

[1]Department of Electrical and Computer Engineering, North Carolina State University, Raleigh, NC 27695, U.S.A.

[2]National Renewable Energy Laboratory, Golden, CO 80401, U.S.A

Abstract

InGaAsP/InGaP quantum well (QW) structures are promising materials for next generation photovoltaic devices because of their tunable bandgap (1.50-1.80 eV) and being aluminum-free. However, the strain-balance limitations have previously limited light absorption in the QW region and constrained the external quantum efficiency (EQE) values beyond the $In_{0.49}Ga_{0.51}P$ band-edge to less than 25%. In this work, we show that implementing a hundred period lattice matched InGaAsP/InGaP superlattice solar cell with more than 65% absorbing InGaAsP well, resulted in more than 2x improvement in EQE values than previously reported strain balanced approaches. In addition, processing the devices with a rear optical reflector resulted in strong Fabry-Perot resonance oscillations and the EQE values were highly improved in the vicinity of these peaks, resulting in short circuit current improvement of 10% relative to devices with rear optical filter. These enhancements have resulted in an InGaAsP/InGaP superlattice solar cell with improved peak sub-bandgap EQE values exceeding 75% at 700 nm, improvement in the short circuit current of 26% relative to standard InGaP devices, and enhanced bandgap-voltage offset (W_{oc}) of 0.4 V.

Index Terms- III-V multijunction solar cells, quantum wells, InGaP, InGaAsP

The inclusion of strain-balanced InGaAsP/InGaP quantum well (QW) in the intrinsic (i) region of InGaP n-i-p structures, can tune the effective bandgap (E_g) of $In_{0.49}Ga_{0.51}P$-based cells into a wide range (1.5-1.8 eV), while maintaining the lattice-matched condition to GaAs substrates [1, 2]. However, strain-balanced InGaAsP/InGaP QW solar cell suffer from inefficient light absorption, resulting in external quantum efficiency (EQE) values beyond the band-edge of $In_{0.49}Ga_{0.51}P$ (hereafter, sub-bandgap EQE) less than 25% and bandgap-voltage offset ($W_{oc} = V_{oc} - E_g$) values higher than 520 mV[1, 2], where V_{oc} is the open circuit voltage. The reported insufficient light absorption in these initial devices is attributed to a few reasons. First, strain-balance limitations have limited the total thickness of the absorbing InGaAsP wells to about 18-25% of the total period thickness [1, 2]. Second, any increase in the well thickness to enhance light absorption will also increase the barrier heights for electrons and holes, and will result in a poor carrier transport [3]. Finally, the number of QWs is limited to 30 periods due to high carbon background doping of $4x10^{15}$ cm^{-3} which corresponds to ~0.7μm depletion region thickness [1, 2, 4].

In this work, light absorption in InGaAsP/InGaP QWs is improved through several strategies. First, the QWs were grown lattice-matched rather than strain-balanced to increase the thickness of the absorbing InGaAsP well relative to that of the barrier. Improvements in both light absorption and carrier collection were achieved by growing a larger percentage of the depletion region occupied by the InGaAsP wells and allowing carrier tunneling through InGaP barriers. Second, the growth of lattice-matched QWs results in less accumulated stress if compared with the strain-balanced structures, and has allowed the growth of 100-period QW device with minimal stress relaxation. Third, light absorption in InGaAsP/InGaP QWs was further improved by etching off the GaAs substrate during processing and depositing a planar back surface reflector (BSR) to double the optical path length [5]. Finally, the use of arsine, phosphine, and triethylgallium precursors resulted in carbon background doping of ~$2x10^{15}$ cm^{-3} [6], which is about half the

corresponding value in the initial devices [1] that used tertiarybutyl-arsine, tertiarybutylphosphine, and trimethylgallium. Reducing the background doping, increased the depletion region to ~1 μm, and allowed the inclusion of 100 depleted QWs (~ 0.8 μm). These changes led to greatly enhanced sub-bandgap peak EQE values above 75% at 700 nm, reduction in the W_{oc} to ~0.4 V and a boost in the short circuit current (J_{sc}) to 20.5 mA/cm^2 which is about 4 mA/cm^2 higher than a standard InGaP device without the QWs.

Samples were grown on (100) GaAs substrates mis-oriented by 2° towards B direction, by metal organic vapor phase epitaxy. A schematic of the InGaAsP/InGaP QWs grown in the *i* layer of $In_{0.49}Ga_{0.51}P$ n-i-p solar cell structure and band-diagram, is shown in Fig. 1. The devices were grown with 20 nm $Al_{0.52}In_{0.48}P$:Se window, 90 nm $In_{0.49}Ga_{0.51}P$:Se emitter, 500 nm $In_{0.49}Ga_{0.51}P$:Zn base, and AlInGaP:Zn back surface field. The QWs were grown lattice-matched at 600 °C, and consisted of alternating layers of $In_{0.32}Ga_{0.68}As_{60}P_{40}$ well (E_g = 1.5 eV) and $In_{0.49}Ga_{0.51}P$ barrier (E_g = 1.85 eV) of thicknesses, t_w = 55-70Å and t_b = 25-32Å, respectively. The devices were grown inverted to allow etching of the GaAs substrate and deposition of a planar gold BSR. Samples were grown with an optional 1.2 μm GaAs filter [Fig. 1] between the absorber and BSR (hereafter, back-filter). Two samples of each device structure were processed separately, with and without etching away the back filter. The back filter absorbs photons in the 1.4-1.85 eV energy range that were not absorbed in the QWs in their first pass, thus simulating the optical environment of the QW cell in a multi-junction. A ZnS (45 nm)/MgF_2 (96 nm) antireflection coating (ARC) was deposited after processing.

Figure 2 shows the EQE of a lattice-matched InGaAsP/InGaP superlattice with different number of periods, at wavelengths beyond the band-edge of $In_{0.49}Ga_{0.51}P$. Three samples were studied: MP159 (t_w = 70 Å, t_b =32 Å, 20-period), MP161 (t_w = 70 Å, t_b =32 Å, 40-period), and MP197 (t_w = 55 Å, t_b =25 Å, 100-period). The slight difference in the period thickness of MP197 was because we found a reduction in the accumulated stress when thinner periods were grown [6].

The total thickness of InGaAsP wells of MP159, MP161, MP197 are 140, 280, 550 nm, respectively, which are about 70% of the total QW region thickness. As shown in Fig. 2, the growth of lattice-matched InGaAsP/InGaP with a larger percentage of the depletion region occupied by InGaAsP, greatly improved the EQE across all wavelengths beyond 680 nm. From the EQE measurements, the one-sun AM1.5 short circuit current contribution of the QWs, $\Delta J_{sc,}$ is shown in Table I. The $\Delta J_{sc,}$ was improved by increasing the number of periods. The 100-period device, with back-filter, exhibits a significantly high absorption in the QW region as shown in Fig. 2, resulting in a ΔJ_{sc} value of 4.37 mA/cm^2, which contributes to about 23% to the total J_{sc} of the device (18.54 mA/cm^2).

Table I. One-sun AM1.5 short circuit current contribution of the QWs ($\Delta J_{sc,}$), effective junction bandgap (E_g), open circuit voltage (V_{oc}), and bandgap-voltage offset (W_{oc}) for the studied samples.

Sample #	Description	ΔJ_{sc} (mA/cm^2) with ARC	E_g (eV)	V_{oc} (V)	W_{oc} (V)
MP159 20-period	Back filter	1.70	1.568	1.176	0.392
	BSR	2.82	1.548	1.173	0.375
MP161 40-period	Back filter	3.08	1.536	1.139	0.397
	BSR	4.67	1.526	1.151	0.375
MP197 100-period	Back filter	4.37	1.543	1.126	0.417
	BSR	5.83	1.528	1.136	0.392

Processing of devices with BSR has improved ΔJ_{sc} as shown in Fig. 2 and Table I. A perfect planar BSR results in an optical path length that is double the physical thickness of the QWs. From table I, ΔJ_{sc} of the 20-period/BSR sample is 2.82 mA/cm^2, which is close to that of the 40-period/back-filter sample (3.08 mA/cm^2). The BSR results in 1.65x, 1.5x, and 1.3x increases in the ΔJ_{sc} values of MP159, MP161, and MP197, respectively. The BSR effect is more significant on MP159 because it is optically-thin (200 nm) and is weakly absorbing the long wavelength photons. The EQE values of the 100-period device (MP197), with BSR, are higher than 70% in the 680-720 nm wavelength range, resulting in a ΔJ_{sc} value of 5.38 mA/cm^2, which contributes to about 26% to

the total J_{sc} of the device (20.54 mA/cm^2). The EQE can be further enhanced by increasing the percentage of absorbing InGaAsP well from 70% to 80-85%, increasing the number of QWs in the depletion region through reducing the carbon background doping to ~10^{14} cm^{-3} [7, 8], and optimizing the carrier transport.

Fig. 2 shows also a comparison between this QW design and previously reported strain-balanced approaches ($In_{0.70}Ga_{0.30}As_{0.10}P_{0.90}$ /$In_{0.40}Ga_{0.60}P$, t_w = 55 Å, t_b = 150Å, 30-period) [2]. The EQE values of lattice-matched 20-period device (MP159), with back filter, are close to those of the strain-balanced structure because the total thickness of the absorbing InGaAsP wells in the two structures is close (~140 nm). However, the total thickness of the QW region in MP159 is 200 nm, which is less than one-third the thickness of the strain-balanced structure (615 nm). Therefore, this indicates that growing the QWs lattice-matched with thicker wells, has allowed thinner structures to achieve the same EQE values as that of the strain-balanced design.

Fig. 3 depicts the EQE of MP159 and MP197 processed with BSR and with back filter, with and without ARC, across the entire wavelengths. The photoluminescence (PL) spectra of these QW structures is also shown in Fig. 3. The inclusion of BSR slightly improves the EQE at wavelengths around 630-680 nm due to enhancing absorption in the $In_{0.49}Ga_{0.51}P$ base because it was grown optically thin (0.5 μm) and is weakly absorbing close to the band-edge. At wavelengths longer than $In_{0.49}Ga_{0.51}P$ band-edge (680 nm), light absorption occurs only in the InGaAsP well. Peaks in the EQE spectra for the QW devices with BSR and without ARC are observed, and are associated with Fabry-Perot resonances. The Fabry-Perot cavity exists due to interference from back and front reflection of photons at the AlGaAs/Au and AlInP/air interfaces with optical reflectance of about ~90% and ~26%, respectively. If the cavity length is integer-multiples of half-wavelengths, photons that were not absorbed in the QWs in their second pass, will interfere constructively with the incident light at resonance wavelengths, λ_{res}. At normal incidence, these $\lambda_{res,}$ can be estimated as follows

$$\lambda_{res} = \frac{2nt}{m + 1/2} \qquad (1)$$

where n is the refractive index, m is the resonance mode order, and t is the thickness of the cavity. Using eqn. (1) and assuming n = 3.5, the resonance modes of the 20-period device (t = 1.064 μm) are estimated to be at: 648 nm at m = 11, 709 nm at m = 10, and 784 nm at m = 9. These calculated values are close to the measured values: 655, 705, 765 nm. The EQE, without ARC, of the 20-period device at the Fabry-Perot resonances, 705 nm and 765 nm, peaks at 63% and 51%, respectively, which are at least 3-times higher than the corresponding values without BSR, as shown in Fig. 3a. Increasing the number of QWs, increases the cavity length and enhance the EQE values at the resonance peaks, as shown in Fig. 3(b). The deposition of MgF_2/ZnS ARC on the samples, with BSR, smears out all these resonance peaks, as shown in the EQE of devices in Fig. 3. The ARC reduces the interference between the incident light and the fraction of reflected photons that were not absorbed in the QWs after their second pass. This is because the front reflectance at the AlInP/ZnS interface is ~3% which is much less than the corresponding value (26%) of the no-ARC case.

The one-sun AM1.5 current density-voltage curve measured for the 100-period device is shown in Fig. 4. The J_{sc}, V_{oc}, fill factor (FF), and η of the back-filter/ARC device were 18.5 mA/cm^2, 1.126 V, 72.3%, and 14.7%, respectively. The corresponding J_{sc}, V_{oc}, FF, and η of the BSR/ARC device were 20.5 mA/cm^2, 1.136 V, 75.3%, and 17.6%, respectively. The reported J_{sc} value here is markedly 26% higher than that of a standard InGaP cell (~1.81 eV), with BSR/ARC [9]. The reason of the J_{sc} enhancement is the sub-bandgap absorption by the QWs as shown in Fig. 3(b). Processing the QWs with BSR improved the J_{sc} by 10.0% relative to the back-filter case. The FF is not high and improving it to 80-85% requires more enhancement of QW interfaces quality and precise stress management to reduce the stress across the QW region [6].

We use the W_{oc} as a figure of merit to evaluate the performance of these QW devices because it evaluates how close the V_{oc} to the fundamental limit set by radiative recombination [10]. The appropriate bandgap to use for QW solar cells can be an ambiguous quantity to determine. We used an effective junction bandgap from a detail-balanced viewpoint based on the EQE as described in [11, 12]. The measured V_{oc}, and calculated bandgaps and W_{oc} at one-sun are given in Table 1. A W_{oc}, approaching or less than 0.4 V, indicates a high solar cell voltage, and the values reported in Table I indicate excellent voltages and high internal and external radiative efficiencies. The W_{oc} slightly increases (V_{oc} slightly decreases) with the increase of well number for a few reasons. First, an increase in the QW region thickness, increases the SRH recombination and increases the dark currents [13]. Second, the unintentional carbon background doping ($2x10^{15}$ cm^{-3}) in the QW region affects the electric field distribution and forms a junction between emitter (n-doped) and QW region (unintentionally p-doped). Increasing the depletion region thickness may lead to the presence of a weak electric field region close to base where carriers are more susceptible to recombination effects, and will increase dark current and may reduce W_{oc} [13]. Third, the possible presence of defects or non-abrupt interfaces at well/barrier and/or barrier/well interface due to arsenic on/off switching may lead to an increase in dark current with the increase of number of interfaces. The dark I-V (DIV) characteristics of the 20-period and 100-period devices, are shown in Fig. 5. The DIV were analyzed using a two-diode model, where the first term with ideality factor n = 1 represents recombination in the quasi-neutral regions, and the second term with ideality factor n = m (1.5 or 2) represents the SRH recombination in the depletion region. The dotted lines in the DIV of figure 5, represent the slope of diodes with ideality factors, n = 1, n = 1.5, and n =2. Analysis of DIV measurements indicates that the performances of 100-period and 20-period devices are dominated by recombination in the depletion region, with n =2 and n=1.5, across the entire I-V sweep, with dark current densities, $J_{o,2} = 4x10^{-9}$ mA/cm^2 and $J_{o,1.5} = 3x10^{-13}$ mA/cm^2, respectively.

We studied the carrier escape mechanisms in this QW design to provide more insights into the EQE improvements shown in Figs. 2-3. Two mechanisms can allow a carrier to escape from QWs and contribute to photocurrent: carrier tunneling and thermionic emission. The competition between carrier escape lifetime ($\tau_{esc.}$) and non-radiative recombination lifetime (τ_r) determines whether the photo-generated carriers are lost or contribute to photocurrent. The probability of carrier escape from a single QW, can be evaluated as follows [14]

$$P = \frac{1/\tau_{esc.}}{1/\tau_{esc.} + 1/\tau_r} \qquad (2)$$

The total probability of carriers escape through the entire QW structure is P^N, for N quantum wells [15].The escape lifetime for tunneling and thermionic emission were evaluated as described in [16] [17]. We used the Anderson's rule to estimate the conduction and valence band and the quantum confined eigenstates were modeled using Kronig-Penney model. Table II summarizes the escape probability for tunneling ($P_{tun.}$) and thermionic emission ($P_{therm.}$) for $n = 1$ electron and heavy-hole states. From Table II, we can conclude that both carrier transport mechanisms exist in the lattice matched structure, with tunneling being more predominant. The tunneling probability for electrons and holes is ~1 due to the thin barriers (25-32 Å) for carriers to tunnel. The P_{therm} for electrons is ~1 due to the fact that only 13% of the total band-offset occur in the conduction band, thus resulting in low barrier height for electrons (0.0684V). The P_{therm} for holes is 0 due to the high effective barrier heights (~ 0.32 V). For the strain-balanced structure [2], the P_{therm} of n=1 electron and heavy hole states are 99% and 58%, respectively and $P_{tun.}$ are zero because of the relatively thick barrier (~150 Å) for carriers to tunnel.

We compared the performance of InGaAsP/InGaP superlattice solar cell to bulk InGaAsP and AlGaAs solar cells. At this initial phase of development, the FF and long wavelength EQE of these QW solar cell structures are lower than bulk InGaAsP and AlGaAs as mentioned earlier. The EQE of QW solar cells (no-BSR) needs to be further improved for future use in multijunction solar

cells as previously discussed. The W_{oc} at one-sun of QW solar cells is ~0.08 V better than that of bulk InGaAsP cells [18, 19] and is similar to AlGaAs cells [20]. The QW structures were grown at temperatures (550-600 °C) less than that of high performance AlGaAs (640 °C) [20] and bulk InGaAsP cells (600-650 °C) [18, 19]. The low-temperature growth may result in less thermal degradation effects on the connecting tunnel junction grown underneath the subcell [21-23]. This work presents an alternative pathway to achieve a 1.5-1.8 eV subcell which is important for several multijunction solar cell approaches.

Table II. Tunneling escape and thermionic emission escape probabilities for electrons and heavy hole states

	$P_{tun.}$		P_{therm}	
	e	hh	e	hh
MP159, 20-period	0.9999	0.9839	0.9999	0.0217
MP161, 40-period	0.9998	0.9629	0.9996	2.8×10^{-6}
MP197, 100-period	0.9998	0.9846	0.9991	8.62×10^{-14}
Strain-balanced structure [2]	0.0	0.0	0.99999	0.5824

In summary, we have improved the sub-bandgap EQE of InGaAsP/InGaP QW solar cell from 25% to higher than 75% at 700 nm. The improvements were realized by modifying the QW design to grow the InGaAsP wells and InGaP barriers lattice-matched with more than 65% absorbing wells; growing a 100-period QW with minimal stress; and removing the substrate during processing and depositing BSR. Strong Fabry-Perot resonance peaks were measured in devices with a BSR but no front antireflective-coating, and the EQE values were highly improved in the proximity of these peaks. The W_{oc} of these QW devices indicates excellent voltages while maintaining efficient carrier transport for both electrons and holes. The J_{sc} is 26% higher than that of a standard InGaP cell.

ACKNOWLEDGMENT

This work was supported by the U.S. Department of Energy Under Contract No. DE-AC36-08GO28308 with the National Renewable Energy Laboratory. S. M. Bedair acknowledges National Science Foundation for financial support. The authors would like to thank Waldo Olavarria and Michelle Young for device growth and processing, and Peter Colter for useful discussions. Islam Sayed acknowledges the support provided by all members of the III/V group at NREL, especially Daniel Friedman, Emmett E. Perl, John Simon, Kevin Schulte, W. E. McMahon, and Ryan France.

References

[1] I. E. Hashem, C. Zachary Carlin, B. G. Hagar, P. C. Colter, and S. M. Bedair, "InGaP-based quantum well solar cells: Growth, structural design, and photovoltaic properties," *Journal of Applied Physics,* vol. 119, p. 095706, 2016.

[2] I. E. H. Sayed, C. Z. Carlin, B. G. Hagar, P. C. Colter, and S. Bedair, "Strain-Balanced InGaAsP/GaInP Multiple Quantum Well Solar Cells With a Tunable Bandgap (1.65–1.82 eV)," *IEEE Journal of Photovoltaics,* vol. 6, pp. 997-1003, 2016.

[3] I. E. H. Sayed, B. G. Hagar, C. Z. Carlin, P. C. Colter, and S. M. Bedair, "Extending the absorption threshold of InGaP solar cells to 1.60 eV using quantum wells: Experimental and modeling results," in *Photovoltaic Specialists Conference (PVSC), 2016 IEEE 43rd*, 2016, pp. 2366-2370.

[4] I. E. H. Sayed, B. G. Hagar, C. Z. Carlin, P. C. Colter, and S. Bedair, "InGaP-based quantum well solar cells," in *Photovoltaic Specialists Conference (PVSC), 2016 IEEE 43rd*, 2016, pp. 0147-0150.

[5] E. Yablonovitch and G. D. Cody, "Intensity enhancement in textured optical sheets for solar cells," *IEEE Transactions on Electron Devices,* vol. 29, pp. 300-305, 1982.

[6] I. E. Sayed, N. Jain, M. A. Steiner, J. F. Geisz, P. Dippo, D. Kuciauskas, P. C. Colter, "In-situ curvature monitoring and X-ray diffraction study of InGaAsP/InGaP quantum wells," *Journal of Crystal Growth,* vol. 475, 2017.

[7] H. Fujii, K. Toprasertpong, H. Sodabanlu, K. Watanabe, M. Sugiyama, and Y. Nakano, "InGaAs/GaAsP superlattice solar cells with reduced carbon impurity grown by low-temperature metal-organic vapor phase epitaxy using triethylgallium," *Journal of Applied Physics,* vol. 116, p. 203101, 2014.

[8] H. Fujii, Y. Wang, K. Watanabe, M. Sugiyama, and Y. Nakano, "Compensation doping in InGaAs/GaAsP multiple quantum well solar cells for efficient carrier transport and improved cell performance," *Journal of Applied Physics,* vol. 114, p. 103101, 2013.

[9] J. F. Geisz, M. A. Steiner, I. Garcia, S. R. Kurtz, and D. J. Friedman, "Enhanced external radiative efficiency for 20.8% efficient single-junction GaInP solar cells," *Applied Physics Letters,* vol. 103, p. 041118, 2013.

[10] King RR, Bhusari D, Boca A, Larrabee D, Liu XQ, Hong W, Fetzer CM, Law DC, Karam NH, "Band gap-voltage offset and energy production in next-generation multijunction solar cells," *Progress in Photovoltaics: Research and Applications,* vol. 19, pp. 797-812, 2011.

[11] M. Steiner, E. Perl, J. Geisz, D. Friedman, N. Jain, D. Levi, G. Horner, "Apparent bandgap shift in the internal quantum efficiency for solar cells with back reflectors," *Journal of Applied Physics,* vol. 121, p. 164501, 2017.

[12] J. F. Geisz, M. A. Steiner, I. Garcia, R. M. France, W. E. McMahon, C. R. Osterwald, *D.* Friedman, "Generalized optoelectronic model of series-connected multijunction solar cells," *IEEE Journal of Photovoltaics,* vol. 5, pp. 1827-1839, 2015.

[13] G. K. Bradshaw, "*Characterization and Analysis of Multi-Quantum Well Solar Cells"*, PhD Dissertation, North Carolina State University, 2014.

[14] J. Nelson, M. Paxman, K. Barnham, J. Roberts, and C. Button, "Steady-state carrier escape from single quantum wells," *Quantum Electronics, IEEE Journal of,* vol. 29, pp. 1460-1468, 1993.

[15] G. K. Bradshaw, C. Z. Carlin, J. P. Samberg, N. A. El-Masry, P. C. Colter, and S. M. Bedair, "Carrier transport and improved collection in thin-barrier InGaAs/GaAsP strained quantum well solar cells," *Photovoltaics, IEEE Journal of,* vol. 3, pp. 278-283, 2013.

[16] D. A. Miller, G. Livescu, J. Cunningham, and W. Y. Jan, "Quantum well carrier sweep out: relation to electroabsorption and exciton saturation," *Quantum Electronics, IEEE Journal of,* vol. 27, pp. 2281-2295, 1991.

[17] H. Schneider and K. v. Klitzing, "Thermionic emission and Gaussian transport of holes in a GaAs/Al x Ga 1− x As multiple-quantum-well structure," *Physical Review B,* vol. 38, p. 6160, 1988.

[18] N. Jain, J. F. Geisz, R. M. France, A. G. Norman, and M. A. Steiner, "Enhanced Current Collection in 1.7 eV GaInAsP Solar Cells Grown on GaAs by Metalorganic Vapor Phase Epitaxy," *IEEE Journal of Photovoltaics,* vol. 7, pp. 927 - 933, 2017.

[19] N. Jain, R. Oshima, R. France, J. Geisz, A. Norman, P. Dippo, D. Levi, M. Young, W. Olavarria, MA Steiner, "Development of lattice-matched 1.7 eV GaInAsP solar cells grown on GaAs by MOVPE," in *Photovoltaic Specialists Conference (PVSC), 2016 IEEE 43rd*, 2016, pp. 0046-0051.

[20] S. Heckelmann, D. Lackner, C. Karcher, F. Dimroth, and A. W. Bett, "Investigations on Al Ga As Solar Cells Grown by MOVPE," *IEEE Journal of Photovoltaics,* vol. 5, pp. 446-453, 2015.

[21] S. Bedair, J. L. Harmon, C. Z. Carlin, I. E. H. Sayed, and P. Colter, "High performance as-grown and annealed high band gap tunnel junctions: Te behavior at the interface," *Applied Physics Letters,* vol. 108, p. 203903, 2016.

[22] S. M. Bedair, J. L. Harmon, C. Z. Carlin, I. E. H. Sayed, and P. Colter, "Annealed high band gap tunnel junctions with peak current densities above 800 A/cm 2," in *Photovoltaic Specialists Conference (PVSC), 2016 IEEE 43rd*, 2016, pp. 2320-2322.

[23] S. Bedair, C. Z. Carlin, J. L. Harmon, I. E. H. Sayed, and P. Colter, "High performance tunnel junction with resistance to thermal annealing," in *AIP Conference Proceedings*, 2016, p. 020003.

Figure Captions

FIG 1: (left) Schematic of lattice matched InGaAsP/InGaP superlattice structure, grown in the unintentionally doped *i* layer in $In_{0.49}Ga_{0.51}P$ n-i-p solar cell structure. Samples were grown with an optional 1.2 μm GaAs filter, and two samples of each device structure were processed separately, with and without etching the GaAs filter. (right) schematic of the energy band diagram, illustrating tunneling and thermionic-emission carrier transports in this structure.

FIG 2: External quantum efficiency (EQE) beyond the band-edge of $In_{0.49}Ga_{0.51}P$ (680 nm) versus wavelength, of InGaAsP/InGaP superlattice solar cell with different number of period. All samples are coated with ZnS/MgF_2. EQE showing improvements over strain balanced InGaAsP/InGaP QW approach.

FIG 3: External quantum efficiency (EQE) and photoluminescence (PL) spectra of (a) 20-period device (MP159) and (b) 100-period device (MP197), with and without ARC, processed with a gold BSR and with back-filter.

FIG 4: Light IV characteristics of 100-period device (MP197), with and without ARC, with a gold BSR and with back-filter.

FIG 5 Dark current voltage characteristics of 20-period QW device (MP159) and 100-period QW device (MP197), with a BSR and with a back-filter. The dotted lines represent diodes with ideality factors n =1, n=1.5, and n=2.

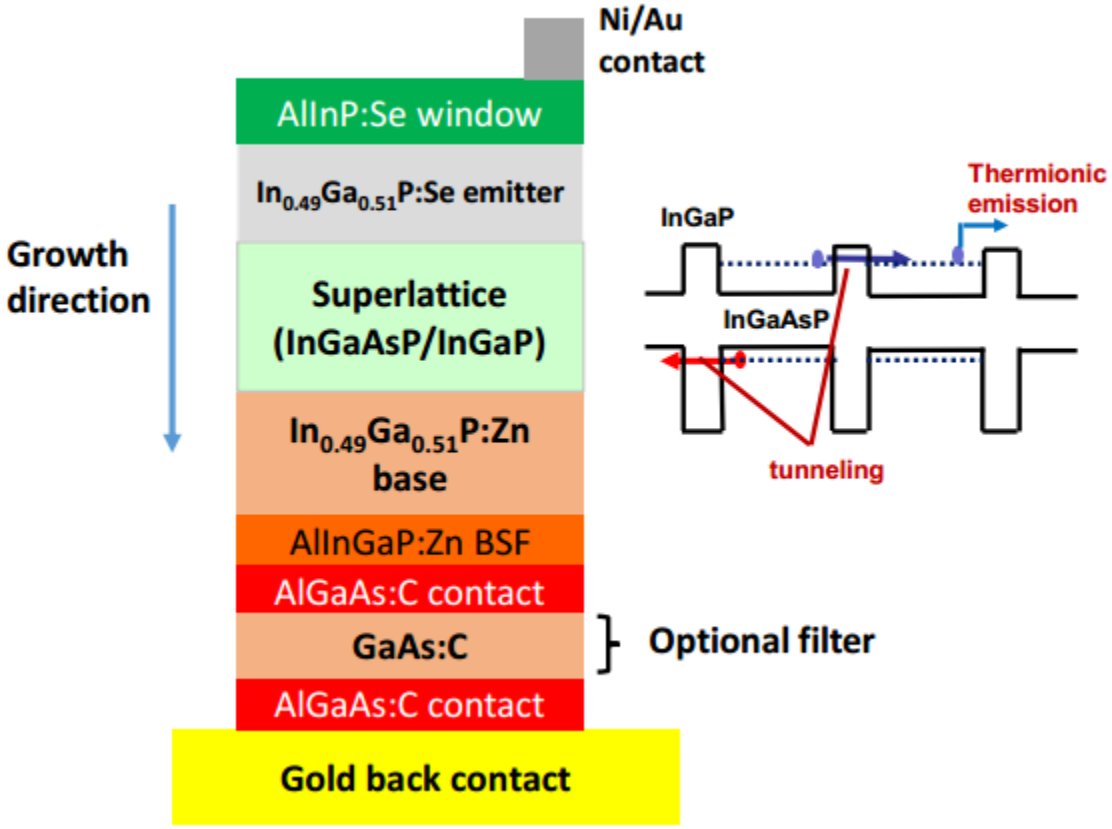

Figure 1

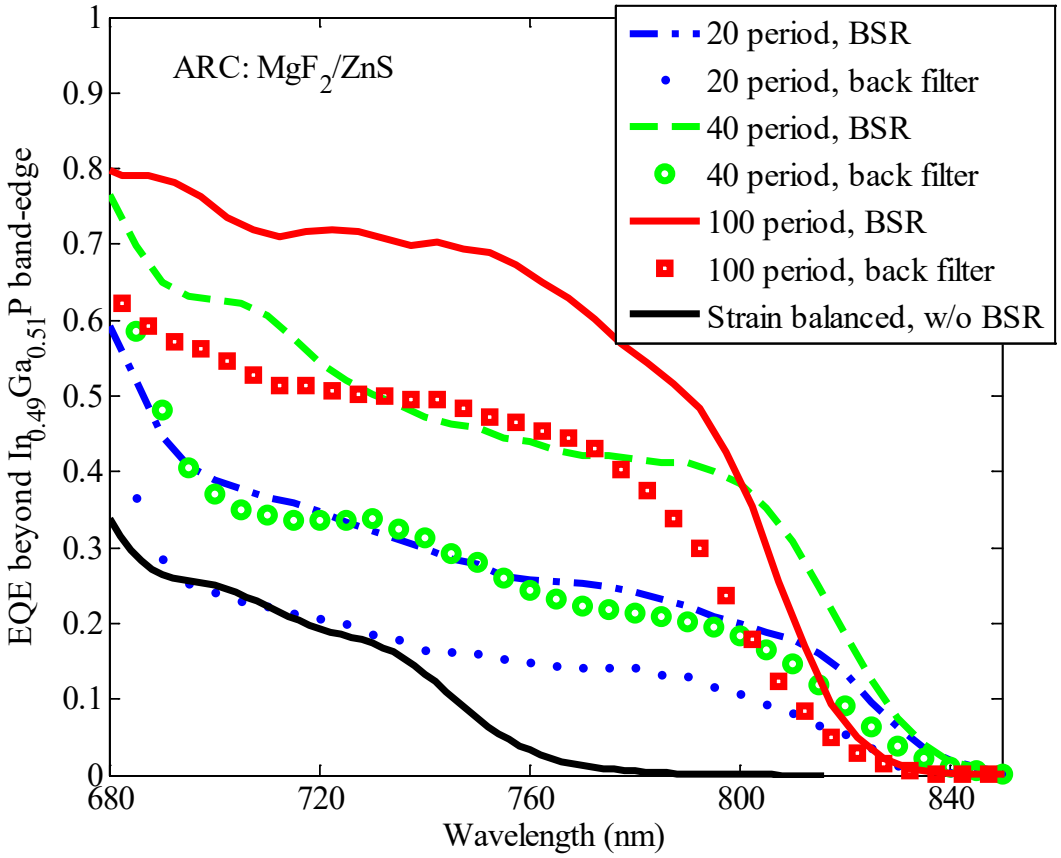

Figure 2

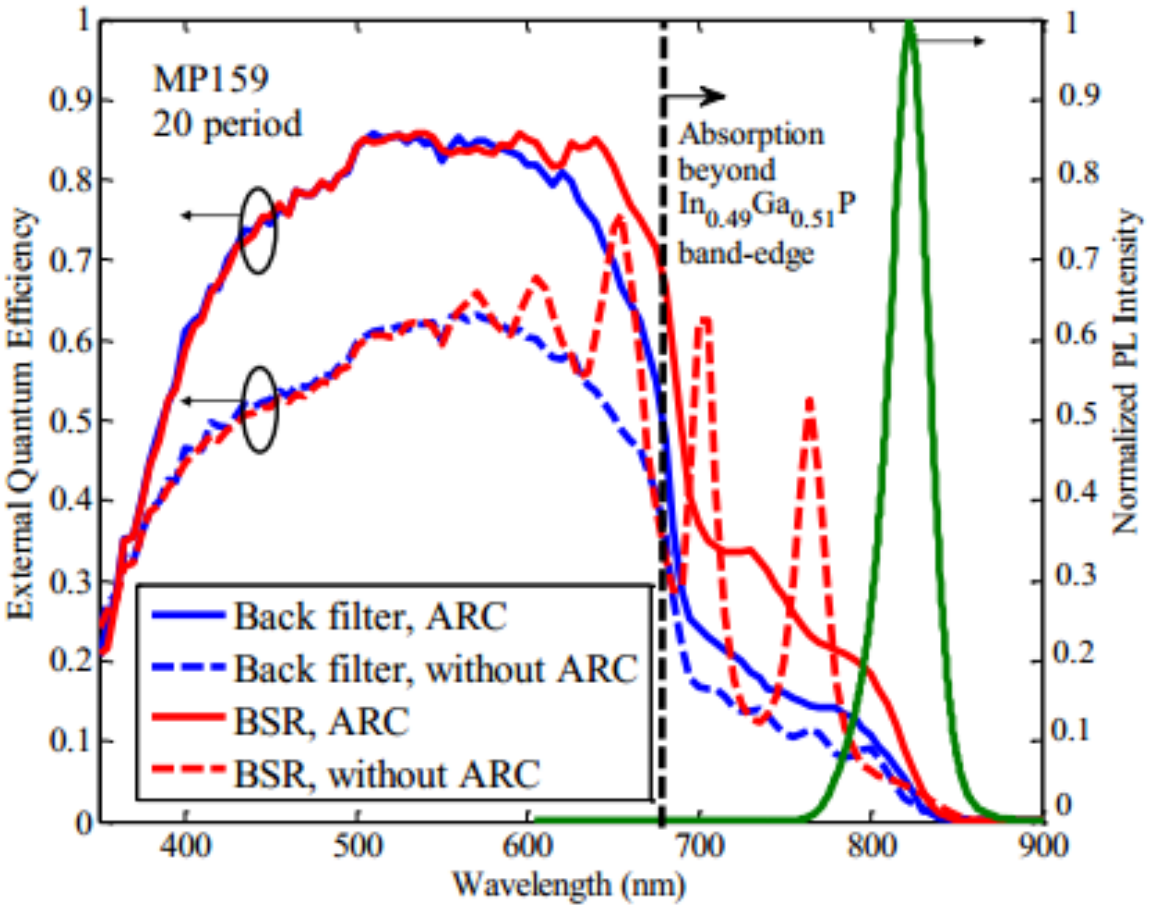

Figure 3(a)

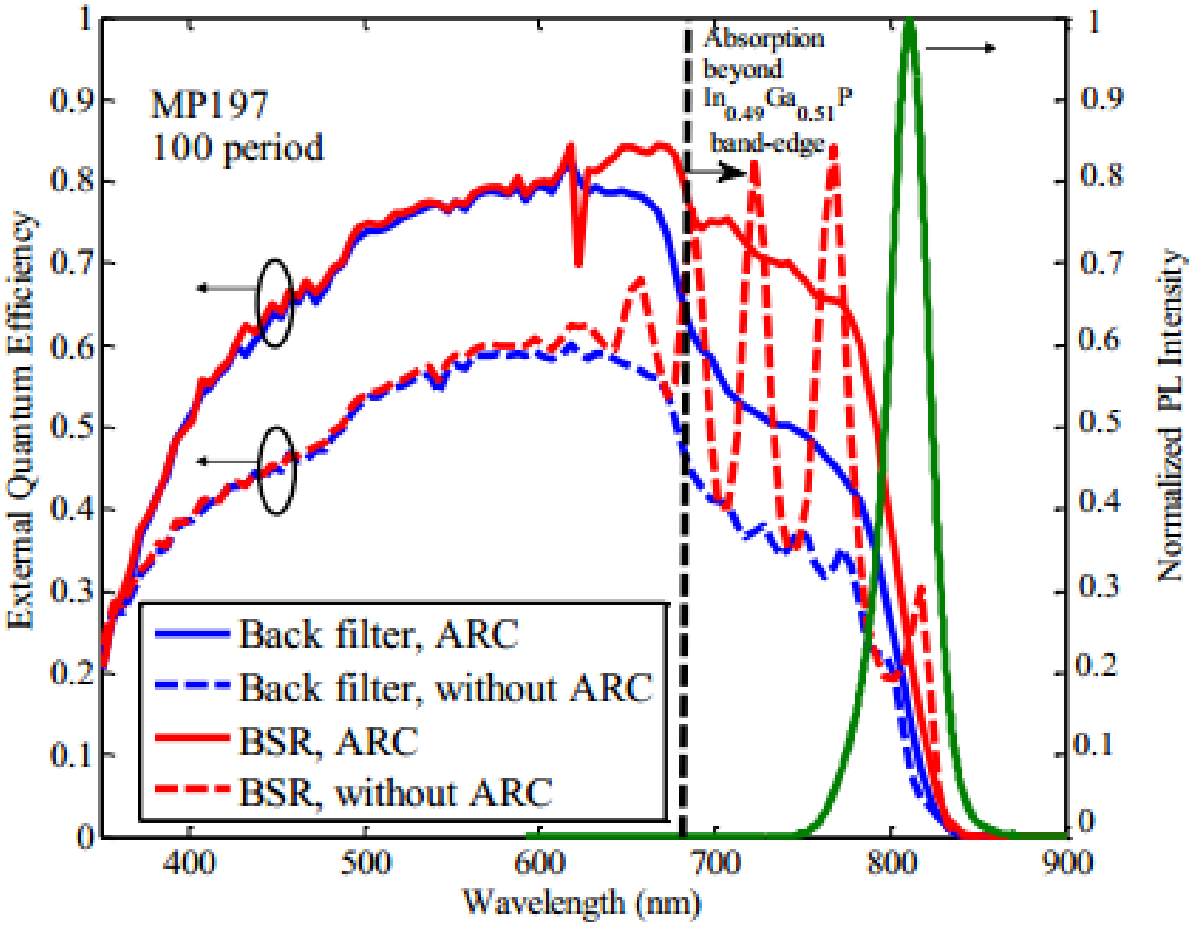

Figure 3(b)

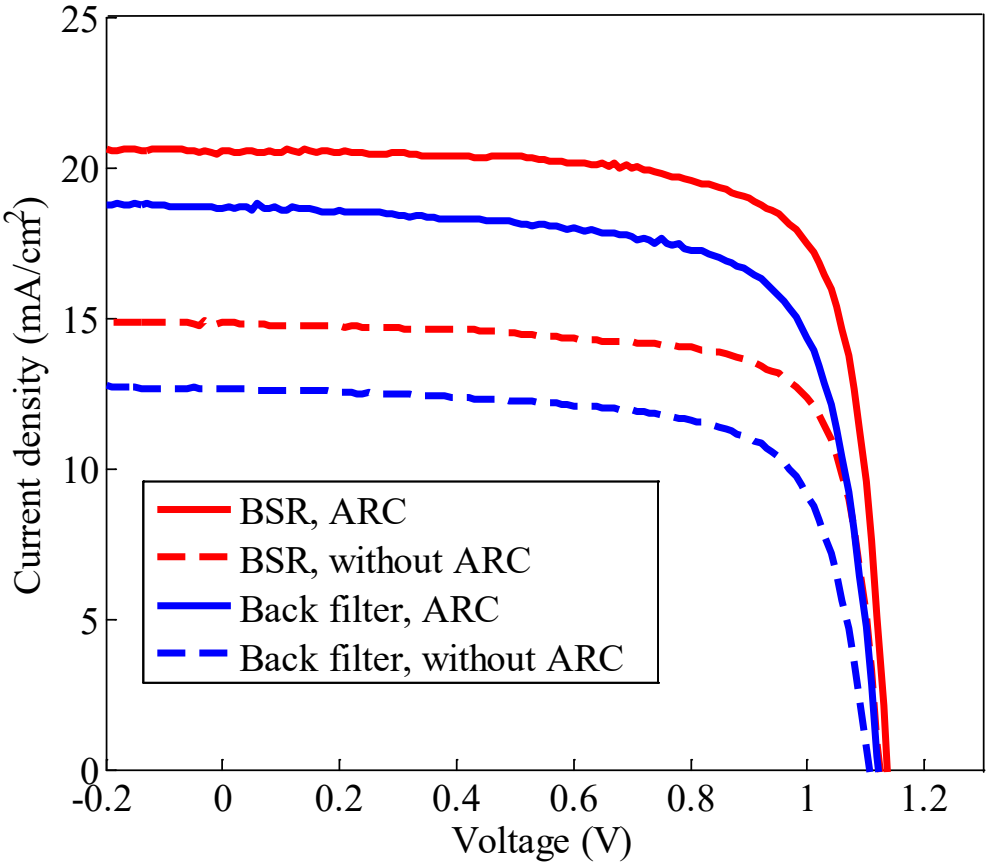

Figure 4

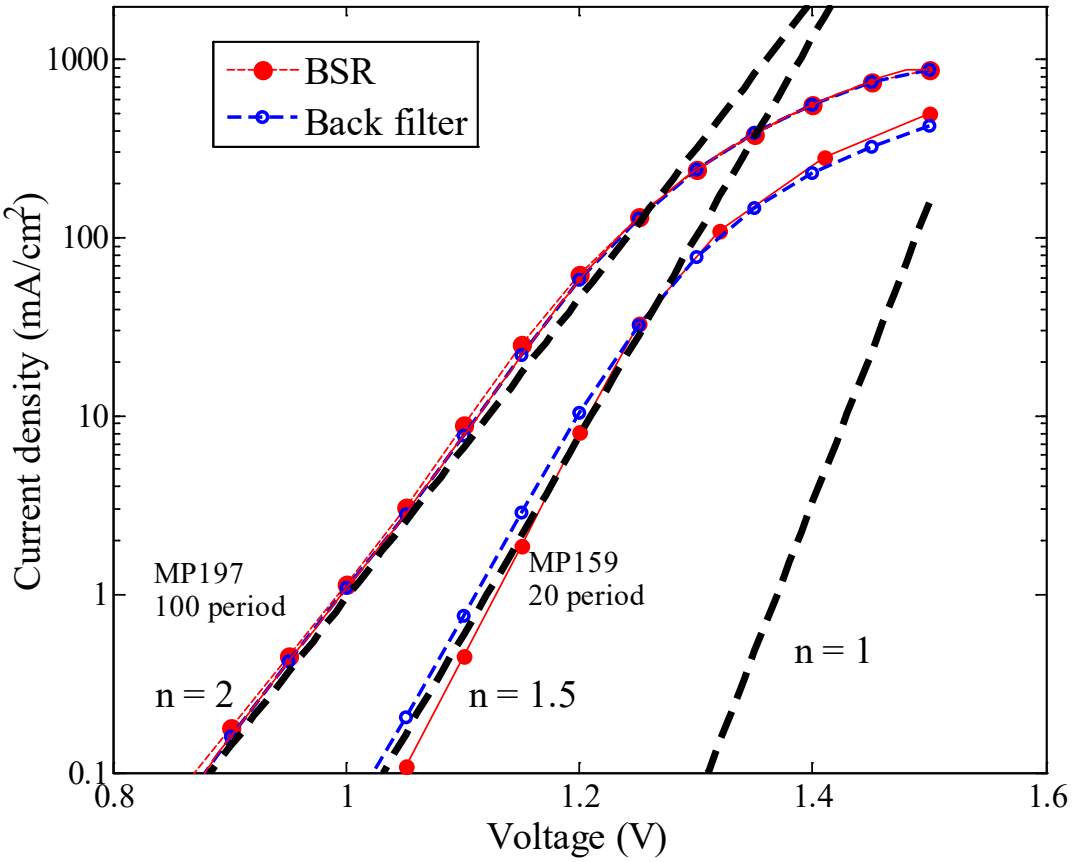

Figure 5